This document is confidential and is proprietary to the American Chemical Society and its authors. Do not copy or disclose without written permission. If you have received this item in error, notify the sender and delete all copies.

Adsorption and Molecular Display of a Redox-active Protein on Gold Nanoparticle Surfaces

Journal:	Langmuir
Manuscript ID	la-2023-01983p.R1
Manuscript Type:	Article
Date Submitted by the Author:	04-Oct-2023
Complete List of Authors:	Hoang, Khoi Nguyen; University of Illinois at Urbana-Champaign, Chemistry Murphy, Catherine; University of Illinois at Urbana-Champaign, Department of Chemistry

SCHOLARONE™ Manuscripts

60

Adsorption and Molecular Display of a Redox-active Protein on Gold Nanoparticle Surfaces

Khoi Nguyen L. Hoang and Catherine J. Murphy*

Department of Chemistry, University of Illinois Urbana-Champaign, 600 South Mathews Avenue, Urbana, Illinois, 61801, USA.

ABSTRACT: Engineered gold nanoparticles (AuNPs) have great potential in many applications due to their tunable optical properties, facile synthesis, and surface functionalization via thiol chemistry. When exposed to a biological environment, NPs are coated with a protein corona that can alter the NP's biological identity but can also affect the proteins' structures and functions. Protein disulfide isomerase (PDI) is an abundant protein responsible for the disulfide formation and isomerization that contributes to overall cell redox homeostasis and signaling. Given that AuNPs are widely employed in nanomedicine and PDI plays a functional role in various diseases, the interactions between oxidized (oPDI) and reduced (rPDI) with 50 nm citrate-coated AuNPs (AuNPs) are examined in this study using various techniques. Upon incubation, PDI adsorbs to AuNP surface, which leads to reduction in its enzymatic activity despite limited changes in secondary structures. Partial enzymatic digestion followed by mass spectrometry analysis shows that orientation of PDI on the NP surface is dependent on both its oxidation state as well as the PDI:AuNP incubation ratios.

INTRODUCTION

Misfolded proteins can lead to loss of functions, but they can also accumulate in large insoluble aggregates that interfere with cellular functions that can lead to cell death, tissue damage, and organ disfunctions.1 Cells solve this problem with a organelle called the endoplasmic reticulum (ER) equipped with protein disulfide isomerase (PDI) to catalyze disulfide formation and isomerization.1 PDI is one of the most abundant proteins in the ER (concentration approaching millimolar range), and it is also found in the nucleus, cytosol, cell surface, and extracellularly.1-4 PDI contains four thioredoxin-like domains abb'a' that adopt a U-shape structure linked by an interdomain region known as the x-linker located between b' and a'. The a and a' domains contain independent active sites that contains two cysteines in the sequence CXXC. These two cysteines can either form an intramolecular disulfide bond (oxidized PDI) or can exists in the dithiol form (reduced PDI). 1-4 Wang et al. have obtained the crystal structure of human PDI in both the reduced and oxidized forms, illustrating the oxidized state (oPDI) has a more open conformation allowing for the entry of substrates and the reduced state (rPDI) has a closed conformation inhibiting their entry.^{2,4}-6 PDI has broad specificity for its substrates and can catalyze disulfide formation and isomerization, depending on the redox states of its active sites (Scheme 1A). PDI catalyzes disulfide formation/reduction by transferring the oxidizing/reducing equivalents to the reduced/oxidized substrate. When incorrect disulfides form, disulfide isomerization is required to convert the non-native disulfides to their native arrangement. The native disulfide isomerization can be achieved via intramolecular rearrangement where the N-terminal cysteine in the active site of PDI

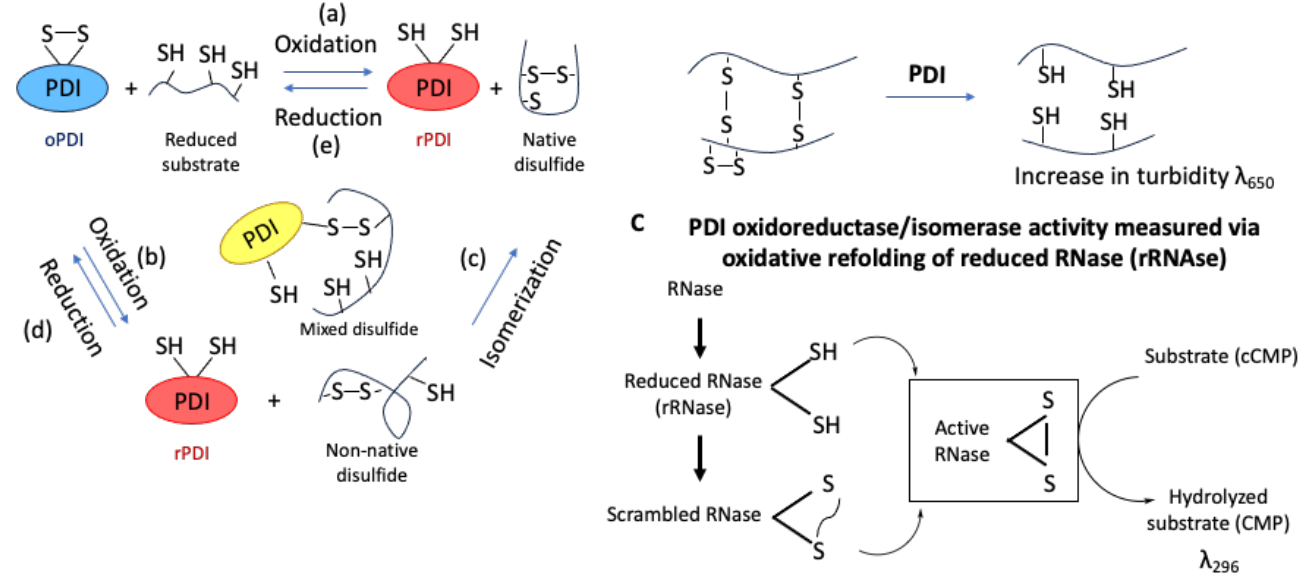
attacks the mispaired disulfide in the substrate and then directly shuffles the disulfides within the substrates, or via a repeated cycles of substrate reduction/reoxidation completed by the mixed reduced/oxidized PDI (**Scheme 1A**).

147

Under normal conditions, PDI reduces the load of misfolded proteins either by its chaperone activity or by correcting disulfide bonds via its isomerization activity. However, PDI can also react noncovalently with peptides and unfolded protein substrates even if they do not contain cysteines; these interactions can prevent substrate-substrate interactions that often leads unfolded proteins to aggregate and become insoluble.7 Under disease states, loss of the normal protective function of PDI as well as gain of additional toxic functions leads to PDI become apoptotic. Under certain conditions, PDI can also facilitate substrate aggregation through disulfide formation.7 For example, PDI is reported to be highly expressed and up-regulated in numerous cancer cell types and PDI supports the survival and progression of several cancers by regulating ER stress, apoptosis, and DNA repair.^{7,8} Knockdown and inhibition of PDI have shown to induce cytotoxicity in human breast cancer, neuroblastoma,9 and melanoma cell lines,10 demonstrating that PDI inhibition is a potential therapeutic strategy for cancer treatment.^{7,11} PDI is also found upregulated in the brain of patients suffering from neurodegenerative diseases like Alzheimer's disease and Parkinson's disease where misfolded proteins accumulate. Some studies have suggested the induction of PDI during ER stress in neurodegenerative diseases reduces the load of misfolded proteins and is, therefore, restoring proteostasis and increasing neuronal viability;12 however, inhibition of PDI suppress apoptosis induced by misfolded proteins¹³ and confers a neuroprotective effect.¹⁴ Inhibition of PDI is also an appropriate strategy for treatment of cardiovascular diseases with a PDI inhibitor currently in clinical trials for the treatment of thrombosis.¹⁵ PDI clearly is a central player in regulating redox homeostasis and

protein folding, which makes the ability to modulate its protective or harmful functions important for the development of therapeutic strategies for various diseases.

A PDI-catalyzed disulfide formation and isomerization B PDI reductase activity measured via insulin reduction



Scheme 1. A) PDI-catalyzed disulfide formation and isomerization. PDI-catalyzed disulfide formation can result in either a native disulfide or a non-native disulfide. The mispaired disulfide can be isomerized by direct intramolecular rearrangement or via a repeated cycle of reduction and reoxidation. Adapted with permission from ref. 4. Copyright 2015 ELSERVIER. (B) PDI reductase activity assay with insulin as a substrate, where increase in turbidity is measured upon reduction of insulin chains. (C) PDI oxidoreductase/isomerase activity assay via oxidative refolding of reduced RNase (rRNase), where PDI-mediated rRNase gain-of-activity is measured by the hydrolysis of RNase substrate, cyclic cytidine monophosphate (cCMP). Adapted with permission from ref. 3. Copyright Frontiers 2014.

Due to their unique size-dependent physicochemical properties, the use of nanoparticles (NPs) in various applications have been growing rapidly.16-19 Specifically, engineered gold nanoparticles (AuNPs) have great potential in health and medicine to improve disease diagnosis and treatment specificity due to their tunable optical and electronic properties as well as ease of functionalization and potential of multifunctionality.20-24 Despite being regarded as nontoxic materials,25 studies have shown that gold nanoparticles can induce apoptosis via oxidative stress.²⁶⁻²⁹ Moreover, upon exposure to biological media, biomolecules such as proteins adsorb to the NPs surface, forming the protein corona which can give the NPs a new biological identity that will determine cellular uptake, biodistribution and toxicity.30-33 PDI has been consistently found in the protein corona upon exposure of several NPs to biological environments, regardless of isolation methods.34,35 One potential mechanism of disturbing redox homeostasis would be to make PDI less bioavailable by adsorption to NP surface; in the case of nonredox active AuNPs, this may be one reason for the generation of reactive oxygen species in various cell lines upon exposure to AuNPs. Therefore, we aim to understand how oPDI and rPDI interact with AuNPs.

EXPERIMENTAL SECTION

Materials. Tetrachloroauric (II) acid trihydrate (HAuCl₄·3H₂O), hydroquinone, protein disulfide isomerase from bovine liver, tris(2carboxyethyl)phosphine hydrochloride (TCEP), dithiothreitol (DTT), insulin from bovine pancreas, sodium phosphate dibasic heptahydrate (Na₂HPO₄·7H₂O), sodium phosphate monobasic monohydrate (NaH₂PO₄·H₂O), ethylenediaminetetraacetic acid (EDTA), hydrogen peroxide, glutathione disulfide (GSSG), glutathione (GSH), guanidine hydrochloride, cytidine 2',3'-cyclic monophosphate (cCMP), ribonuclease A from bovine pancreases (type III A), sodium phosphate dibasic heptahydrate (Na₂PO₄·7H₂O), sodium phosphate monobasic monohydrate (NaH₂PO₄·H₂O), and (tris-acetate) were purchased from Sigma. Trisodium citrate dihydrate (Na₃C₆H₅O₇·2H₂O) was purchased from Flinn Scientific.

Synthesis of 50 nm AuNPs. 50 nm AuNPs were synthesized via the Chan method. 36 Briefly, gold seeds solution was first prepared by bringing a mixture of $300~\mu L$ of 1%~w/v HAuCl $_4$ · $3H_2O$ and 30~mL of nanopure H_2O to a boil while stirring before adding $900~\mu L$ of trisodium citrate dihydrate (1%~w/v). The solution was removed from the heat after the formation of seeds are completed, as indicated by the color transition (after 10~minutes). To the 6.5ml of gold seeds, a mixture of 2.5~mL of HAuCl $_4$ · $3H_2O$ (1%~w/v) and 245~mL of nanopure H_2O was added while

stirring at room temperature. Then, 550 μ L of trisodium citrate dihydrate (1% w/v) and 2.5 mL of hydroquinone (0.03 M) were added to the solution simultaneously. The solution was allowed to stir for 1 hour before centrifugation at 600 xg for 20 minutes to purify and was then resuspended in water.

AuNP characterization. Hydrodynamic light scattering and ζ-potential of the NPs were measured using a Malvern Zetaseizer Nano ZS. Extinction spectra was collected using an Agilent Technology Cary 5000 UV-vis-NIR spectrometer. Transmission electron microscopy (TEM) micrographs of the NPs in water were obtained by drop-casting onto a copper grid with carbon type-B 300 mesh (01813-F, Ted Pella) before imaging on JEOL 2100 Cryo TEM with LaB₆ emitter operated at 300 keV. Characterization data for the 50 nm AuNPs can be found in the SI: TEM micrographs (**Figure S1A**), hydrodynamic size and ζ-potential (**Figure S1B** and **Figure S1C**).

Preparation of oxidized (oPDI) and reduced (rPDI) forms of protein disulfide isomerase (PDI). The oPDI stock (1000 μ g/mL) was prepared by dissolving as-purchased oPDI from bovine liver in 10 mM sodium phosphate buffer. In contrast, the rPDI stock (1000 μ g/mL) was prepared by dissolving as-purchased PDI from bovine liver in 10 mM sodium phosphate buffer containing 1 mM TCEP (1:10 protein:TCEP molar ratio) and left to incubate for 30 minutes before usage.

Dynamic light scattering (DLS) titrations of PDI with AuNPs. Titration curves were made using samples containing 0.005 nM AuNPs and oPDI/rPDI in the range of 0 to 350 μ g/mL concentration in 10 mM sodium phosphate buffer after 1 hour of incubation on ice. Each titration point was prepared in a separate centrifuge tube in triplicate. DLS was also used to characterize the samples after 1x centrifugation (500 xg, 10 minutes).

Circular dichroism spectroscopy. Circular dichroism spectra were collected for 100 $\mu g/mL$ oPDI/rPDI free protein and 100 $\mu g/mL$ oPDI/rPDI after incubating with 0.01 nM AuNPs on a Olis DSM 17 CD spectrometer. Each spectrum was an average of 5 scans collected from 260 nm to 190 nm (in increment of 0.2 nm) at 25°C, which was baseline subtracted and smoothed using a 50-point Savitzky-Golay filter. Secondary structure estimation was conducted using DichroWeb CDSSTR analysis and protein Reference Set 7.37.38

PDI reduction activity assay with insulin as a substrate. The PDI reduction activity assay was performed with insulin as the substrate via a high-throughput assay reported by Smith $et~al.^{39}$ with modifications for 96-well plates. For control wells, the reactions mixture of enzyme (oPDI/rPDI): insulin (33 µg/mL: 0.16 mM final concentration) was added to the assay buffer (100 mM sodium phosphate and 0.2 mM EDTA, pH 7.0). For AuNPs-exposed wells, the same amount of oPDI/rPDI was first incubated with adjusted concentration AuNPs to reflect the PDI:citAuNP ratio from DLS titration experiment (15 µg/mL PDI: 0.005 nM AuNP) before mixing with insulin substrate. The enzyme (oPDI/rPDI) and substrate

(insulin) were allowed to incubate for 10 minutes before DTT (1mM final concentration) was added and allowed to proceed for 30 minutes before the reaction was stopped by adding H_2O_2 (125 mM final concentration). For positive control wells, the H_2O_2 was added to the wells before adding the enzyme:substrate mixture. The optical density of each well was measured at 650 nm on the SpectraMax M2 Multimode Microplate Reader (VWR) at room temperature. The residual activity (%) of the enzyme reaction in the presence of AuNPs is calculated as follows:

$$\% activity = \frac{(\textit{OD}_{\textit{PDI}+NP} - \textit{OD}_{\textit{NP}} - \textit{OD}_{\textit{positive control}})}{(\textit{OD}_{\textit{control}} - \textit{OD}_{\textit{positive control}})} \, (\text{Eq. 1})$$

where OD_{PDI+NP} , $OD_{control}$, $OD_{positive\ control}$ is the optical density measurement for insulin aggregation in presence of AuNP-exposed PDI, free PDI, and free PDI +H₂O₂, respectively, OD_{NP} is the optical density measurement to account for AuNP background. The general scheme is shown in **Scheme 1B**.

PDI oxidative refolding activity assay with scrambled/reduced RNase as a substrate. The RNase activity assay is adapted from the procedure reported by Lyles et al.40 RNase was reduced and denatured (rRNase) by incubating 5 mg of native RNase in 1 mL of 0.1 M trisacetate (pH 8.0) containing 2 mM EDTA, 6 M guanidine hydrochloride, and 0.14 M DTT. The rRNase was then filtered using a AMICON filter immediately before use. The concentrations of cCMP and RNase (native and reduced) were determined spectrophotometrically at 296 nm for cCMP $(\epsilon = 0.19 \text{ mM}^{-1} \text{ cm}^{-1})$ and 277.5 nm for RNase $(\epsilon = 9.8 \text{ mM}^{-1})$ cm⁻¹ for native, and ϵ =9.3 mM⁻¹ cm⁻¹ for reduced). For positive control wells, cCMP (1.125 mM), GSH (0.25 mM), GSSG (0.05 mM), and PDI (0.35 µM) were mixed before adding RNase (2.1 µM). For negative control wells, rRNase was added instead of RNase. AuNPs-exposed PDI samples were prepared by first incubating AuNPs with oPDI/rPDI for 1 hour on ice (15 $\mu g/mL$ PDI: 0.005 nM AuNP) before adding to reaction mixture with rRNase. Uncatalyzed reactions (without addition of PDI) were also monitored in parallel under identical conditions. The reactions were monitored at 296 nm over 45 minutes at 37 °C using SpectraMax M2 Multimode Microplate Reader (VWR). Gold NP background was subtracted before reporting final results. The general scheme is shown in **Scheme 1C**.

Enzymatic digestion of PDI from the surface of AuNPs. oPDI and rPDI was incubated with AuNPs at both 15 μ g/mL PDI: 0.005 nM AuNP and 300 μ g/mL PDI: 0.005 nM AuNP on ice while shaking. After 1 hour incubation, the NP-protein complexes were centrifuged 1x at 500 xg for 10 minutes. Free oPDI, free rPDI, and the isolated NP-protein corona complexes were then digested with trypsin (1:50 enzyme:protein) for 1 hour at 25°C.

Proteomic analysis. The AuNPs that were exposed to oPDI/rPDI per the previous paragraph were then removed by centrifugation and the digested protein corona samples were desalted using StageTips. The lyophilized samples were then resuspended in 0.1% formic acid (FA)/5% acetonitrile (ACN) (50 ng from each sample, measured by the

BCA assay (Pierce) for injection into UltiMate 3000 nanoLC and analyzed by a Q Exactive HF-X high resolution mass spectrometer (Thermo Scientific). The peptides were separated using a 25 cm Acclaim PepMap 100 C18 column (Thermo Scientific) and mobile phases of 0.1% FA in water (mobile phase A) and 0.1 %FA in 80% ACN (mobile phase B) at a flow rate of 300 nL/min. The gradient started at 5% B, which was then increased to 35% B over 60 minutes, and then increased to 55% B over 5 more minutes; this was followed by column washing and equilibration. The column was maintained at 50 °C over the course of the run. Full MS scans from 350-1500 m/z were acquired at 120k resolution in the Orbitrap, followed by high energy collision dissociation of the 20 most abundant ions. MS scans were acquired at 15k resolution. Mass spectra were analyzed using MaxQuant software version 2.0.1.0 containing the Andromeda search engine. The spectra were searched against the Bos taurus Uniprot sequence database. Trypsin was specified as the enzyme with a maximum of 2 missed cleavages; minimum peptide length was 5. The modifications of oxidation and N-terminal acetylation was included in the search. The precursor mass tolerance was 10 ppm, and the fragment mass tolerance was 20 ppm. The match between runs function was enabled with a match time window of 1 minute. The false discovery rate was set to 1% at the PSM and protein level. Label-free quantitation was done with MaxQuant41,42 using a minimum ratio count of 1. Only fragments that were quantified (having a reported LFQ intensity value) in at least 2 out of the three replicates in at least one condition were analyzed. The digestion pattern was plotted using an average log2-transformed LFQ intensity of each fragment detected in replicates for each condition (Figure S3 and Figure S4). The fold change difference in digestion between bound and free protein samples were calculated by taking log₂ of the ratio between the sum of the LFQ intensities of all fragments associated with a specific cut site detected in bound samples and the sum of the LFQ intensities of all fragments associated with the same cut site detected in free samples.

RESULTS AND DISCUSSION

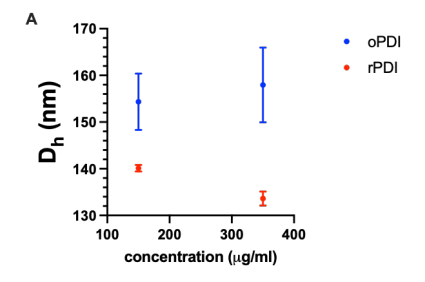
Dynamic light scattering (DLS) titration of PDI with AuNPs to obtain binding constants. The AuNPs were synthesized via the Chan method,36 producing gold spheres with diameters ~50 nm (as measured by TEM, Figure **S1A**) that have hydrodynamic diameters of 55.0 \pm 0.1 nm and a ζ -potential of -44.7 \pm 4.1 mV (as measured by the Zetasizer, Figure S1B and Figure S1C). We measured the hydrodynamic diameters of the free oPDI, free rPDI, and titrations of PDI into AuNPs in 10 mM phosphate buffer. Data for oPDI is shown in blue, whereas data for rPDI is shown in red (Figure 1). The hydrodynamic diameter was measured for oPDI to be 154.3 ± 6.0 nm at $150 \mu g/mL$ and 157.9 ± 6.0 nm at 350 µg/mL (**Figure 1A**). The hydrodynamic diameter was measured for rPDI to be 140.1 ± 0.7 nm at 150 μ g/mL and 133.6 ± 1.5 nm at 350 μ g/mL (Figure 1A). The free oPDI samples have larger hydrodynamic diameters in comparison to free rPDI samples, which is

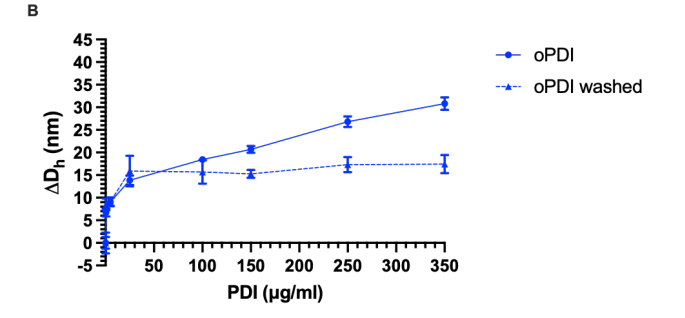
consistent with the open and closed conformation reported in the literature. 2,5,6 The hydrodynamic diameter values, however, are greater than expected for both free oPDI and rPDI. In particular, recombinant human oPDI has been determined to have dimensions of $16.1 \times 3.4 \times 15.7$ nm and recombinant human rPDI to have dimensions of $3.8 \times 10.1 \times 12.4$ nm via X-ray diffraction (XRD). 5 The free proteins are likely to be aggregating via dimerization in solution (**Figure S2E**).

Titration of increasing concentrations of oPDI (Figure 1B, S2A,C) and rPDI (Figure 1C, S2B,D) into AuNPs showed an increase in AuNPs hydrodynamic diameters, indicating protein binding. We can estimate an overall binding constant from the DLS data by fitting into a Langmuir adsorption isotherm $model^{43,44}$

$$\frac{\Delta D}{\Delta D_{max}} = \frac{K_a[PDI]}{1 + K_a[PDI]} \text{ (Eq. 2)}$$

where ΔD and ΔD_{max} are the change and maximum change in NP diameter, K_a is the association constant, and [PDI] is the concentration of PDI at each DLS titration point. Assuming homogeneous single layer PDI adsorption onto AuNPs, an overall binding constant of $(8.1\pm6.1) \times 10^6 \, \mathrm{M}^{-1}$ for oPDI and $(9.7\pm3.3) \times 10^6 \, \mathrm{M}^{-1}$ for rPDI was obtained.





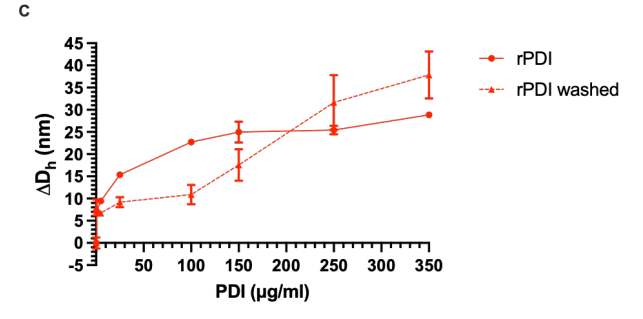
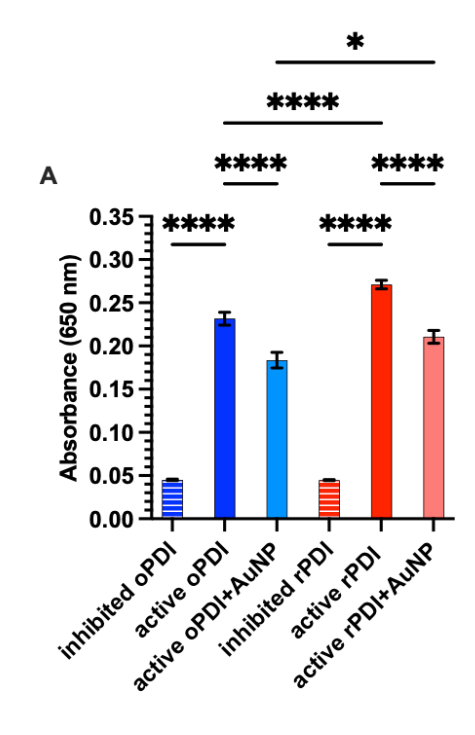


Figure 1. Dynamic light scattering results for (A) free oPDI (red) and rPDI (blue), and titration curves for (B) oPDI and (C) rPDI into 0.005 nM AuNPs for as incubated samples (circle) and 1x wash samples (triangle). Error bar for each titration point represents

standard deviation from 3 replicates (3 DLS measurements/replicate).

Upon oPDI in situ titration into AuNPs, the hydrodynamic diameters of AuNPs saw an initial increase of ~ 15 nm at low oPDI concentration, which gradually increased to ~30 nm at high oPDI concentration (Figure 1B, solid blue line). At each titration point, 1x washing of the protein-NP complexes reveals a more obvious plateau, at ~15 nm thickness (Figure 1B, dashed blue line). This suggests that oPDI adsorbed to the AuNP in a multi-layered fashion in situ, and the soft corona oPDI was removed with 1x centrifugation to leave an approximately 15 nm-thick oPDI hard corona layer. Similarly, in situ titration of rPDI into AuNPs also resulted in an increase to the AuNPs hydrodynamic diameters, where there is an increase of ~15 nm at low rPDI concentration and gradually increased to ~30 nm at high rPDI concentration (**Figure 1C**, solid red line). However, the 1x washing at each titration point appeared to be more complex for rPDI samples. The apparent protein thickness is lowered at low rPDI concentration (~10 nm) while being higher (>30 nm) at high rPDI concentration, suggesting complex protein-protein interactions (Figure 1C, dashed red line). These results indicate that redox state of PDI and protein:NP incubation ratios play a role in the adsorption of the protein on the NP surface. It is interesting that incubation with oPDI did not induce a significant different increase in AuNPs' hydrodynamic diameters compared to incubation with rPDI, considering the larger hydrodynamic diameter of free oPDI (Figure 1A). This also contrasts the observation made by Zheng et al.,45 where they observed the hydrodynamic diameter of 40 nm AuNPs increased more upon adsorption of human recombinant oPDI in comparison to human recombinant rPDI. The discrepancy can potentially be due to the different protein sources or their usage of DTT, a thiol, as reducing agent instead of TCEP in our study.

PDI reductase activity. The activity of PDI while bound to AuNPs was examined by adapting the end-point insulin reduction assay (Scheme 1B) developed by Smith et al.39 Briefly, free oPDI/rPDI and AuNP-exposed oPDI/rPDI (15 μg/mL PDI: 0.005 nM AuNP) were allowed to interact with insulin for 10 minutes before adding DTT to kickstart the aggregation curves before adding H₂O₂ to arrest the reaction, where the absorbance of each well was measured at 650 nm on the plate reader. The background subtracted absorbance is shown in Figure 2A and the calculated activity % in comparison to its free PDI control is shown in Figure 2B. As seen in Figure 2A, initial addition of H₂O₂ prevents both oPDI (inhibited oPDI) and rPDI (inhibited rPDI) from reducing insulin, demonstrated in the lack of insulin aggregation or turbidity. In the absence of initial H2O2 addition, both oPDI and rPDI cause formation of insulin chain aggregation, shown in the increase of turbidity. There is a significant higher level of turbidity seen in free rPDI (active rPDI) sample in comparison to free oPDI (active oPDI) samples, which is reasonable considering the redox state of the active sites. The turbidity measurements for AuNP-exposed samples, which were corrected for the contribution from NPs, show significant reduction in comparison to its corresponding control. Interactions with AuNPs reduces both oPDI and rPDI ability to reduce insulin down to around 75% (**Figure 2B**). The loss of activity suggests that adsorption to AuNPs affect the conformation of PDI (regardless of oxidation state) or that the NPs are blocking the active sites, or the combination of the two.



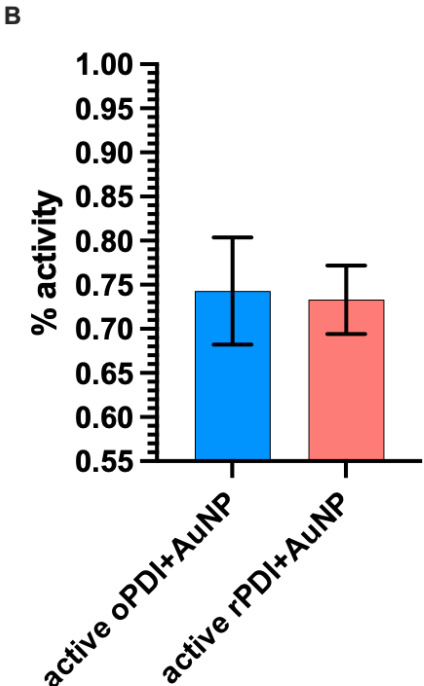


Figure 2. Insulin reduction activity assay. (A) End-point turbidity measurements for oPDI (blue) and rPDI (red) of inhibited PDI (horizontal stripes), active PDI (dark solid color), and AuNP-exposed active PDI (light solid colors). Stop agent, H2O2, was added at the beginning for inhibited PDI, and at the end for active PDI and AuNP-exposed active PDI samples. (B) Calculated residual

activity (%) of PDI after exposure to AuNPs. All samples contain the same concentration of PDI with AuNP added at a ratio of 15 μ g/mL PDI: 0.005 nM AuNP. Error bars represent the errors of the means with n=16. Asterisks denote statistically significant difference using one-way ANOVA followed by Dunnett's multiple comparisons performed on raw absorbance at 650 nm, * for p=0.0494, **** p<0.0001.

PDI oxidoreductase/isomerase activity. While PDI reduces insulin and leads to increase in turbidity due to insulin aggregation, it promotes oxidative refolding in a series of thiol oxidation/reduction cycles and possibly isomerization reactions to promote gain-of-function for reduced, inactive RNase (rRNase).3 Thus the oxidoreductase/isomerase activity of PDI can then be measured based on the measurement of activity of the recovered, refolded RNase. In brief, RNase is reduced in denaturing conditions to acquire random disulfide bonds before being introduced to PDI in glutathione/glutathione disulfide (GSH:GSSG) redox buffer to measure the recovered RNase activity via the hydrolysis of its substrate cyclic cytidine monophosphate (cCMP).40 Figure 3A shows the RNase mediated cCMP cleavage reactions with native RNase (active RNase), reduced RNase (inactive RNase), active PDIcatalyzed refolded rRNase (inactive RNase + active PDI), and (AuNP-exposed PDI)-catalyzed refolded rRNase (inactive RNase+ active PDI + AuNP), in which RNase reactions were background subtracted and all PDI-catalyzed reactions were corrected for the uncatalyzed rate of oxidative refolding observed in parallel reactions in absence of PDI. The hydrolysis of cCMP results in the increase in absorbance at 296 nm at a reasonably linear, steady state velocity for native RNase (active RNase), whereas there is a lag for reduced/scrambled RNase (inactive RNase) or a burst in regain of RNase activity in presence of PDI. Lags are common for reduced/scrambled RNase due to the prerequisite formation of RNase redox isomers that can be converted to the native protein.40 The time to reach half-maximum absorbance at 296 is calculated and plotted in Figure 3B. Overall, rRNase is less efficient at hydrolyzing cCMP in comparison to native RNase and that PDI can aid rRNase in refolding to regain some native function. Free oPDI is more efficient in rRNase refolding in comparison to free rPDI. Exposure to AuNP at 15 μg/mL oPDI: 0.005 nM AuNP ratio seems to enhance oPDI in aiding rRNase refolding, whereas exposure to AuNP at 15 μg/mL rPDI: 0.005 nM AuNP ratio seems to weaken rPDI in aiding rRNase refold-

Characterization of conformation and orientation of PDI on AuNPs. Adsorption to AuNPs alters both reductase and oxidase activity of PDI as shown Figure 2 and Figure 3. Hence, circular dichroism (CD) was then utilized to monitor the change in protein secondary structures upon binding to AuNPs. The CD signal was measured for both free oPDI and rPDI, as well as AuNP-exposed oPDI and rPDI and the smoothed average of 3 replicates is shown in Figure 4A. There is a clear difference in the CD spectra between oPDI (blue) and rPDI (red), also reported by Guyette et al.46 However, there is not a significant

difference in CD spectra between free vs. bound samples (dotted vs. solid). The smoothed CD curves were then analyzed using DichroWeb CDSSTR method (with protein Reference Set 7) to give % of total secondary structures shown in Figure 4B. In all samples, alpha helix is the major secondary structure, followed by random coil and beta sheet. There is a reduction in β -sheet % in rPDI samples compared to oPDI samples; however, there is not a significant difference in the secondary structures' distribution between free vs. bound samples. Under the incubation condition of 25 µg/mL PDI: 0.005 nM AuNP, the particle surface should be saturated with proteins as indicated by DLS titration (Figure 1) with limited portion of the protein is free in solution. Hence, it can be concluded that adsorption onto AuNPs does not significantly modify secondary structures of either oPDI or rPDI.

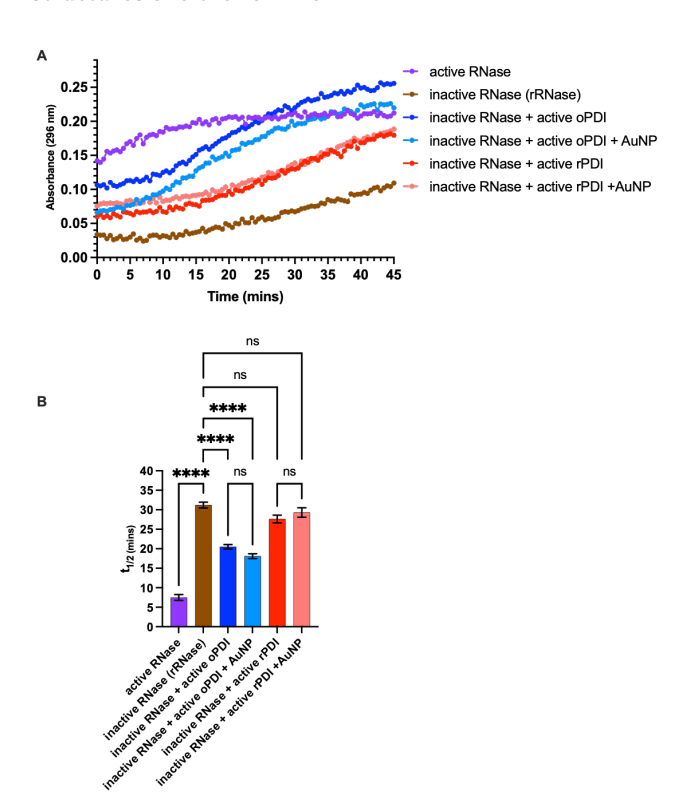
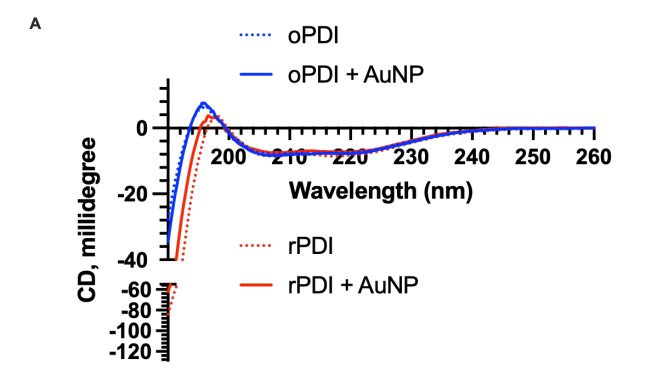


Figure 3. Refolding RNase activity assay. (A) Kinetics of RNasemediated hydrolysis of cCMP with native RNase (active RNase, purple), reduced RNase (inactive RNase (rRNase), brown), inactive RNase in presence of active oPDI (inactive RNase + active oPDI, dark blue), inactive RNase in presence of AuNP-exposed active oPDI at 15 µg/ml oDPI: 0.005 nM AuNP (inactive RNase +active oPDI + AuNP, light blue), inactive RNase in presence of active rPDI (inactive RNase +active rPDI, dark red), and reduced RNase in presence of AuNP-exposed active rPDI at 15 μg/ml rDPI: 0.005 nM AuNP (inactive RNase +active rPDI +AuNP, pink). The curves are averaged from 6 replicates, error bars are not shown for clarity, (B) Calculated time to reach half maximum absorbance at 296 nm from kinetics of RNase-mediated hydrolysis of cCMP with native RNase (active RNase, purple), reduced RNase (inactive RNase (rRNase), brown), inactive RNase in presence of active oPDI (inactive RNase + active oPDI, dark blue), inactive RNase in presence of AuNP-exposed active oPDI at 15 μg/ml oDPI: 0.005 nM AuNP (inactive RNase +active oPDI + AuNP, light blue), inactive RNase in presence of active rPDI (inactive RNase +active rPDI, dark red),

60

and reduced RNase in presence of AuNP-exposed active rPDI at 15 μ g/ml rDPI: 0.005 nM AuNP (inactive RNase +active rPDI +AuNP, pink). Error bars represent standard error of the mean. **** p<0.0001 using one-way ANOVA, Turkey's multiple comparisons test.



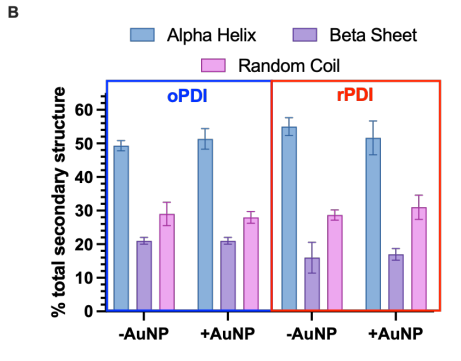


Figure 4. Characterization of PDI secondary structures on AuNPs surface. (A) Smoothed CD spectra for oPDI (blue) or rPDI (red) free in solution (dotted line) or incubated with AuNPs at 25 µg/ml PDI: 0.005 nM AuNP ratio. Each spectrum shown is the average of 3 replicates for each condition. Error bars are now shown for clarity. (B) Corresponding calculated secondary structures using DichroWeb. Each point represents a calculated value for each replicate. Error bars represent standard deviation, n=3.

A partial enzymatic digest followed by mass spectrometry (MS) analysis⁴⁴ of the released peptide fragments was conducted to probe the orientation of PDI on the surface of AuNPs. To further inspect the discrepancy in adsorption between oPDI and rPDI as seen in DLS titration (Figure 1), we exposed AuNPs to oPDI and rPDI at 15 μg/mL: 0.005 nM AuNP and at 300 µg/mL: 0.005 nM AuNP, then removed excess proteins with 1x centrifugation (500 xg, 10 minutes) before incubating them with a trypsin, the chosen digestive enzyme. To facilitate a partial digestion condition, a low enzyme: protein ratio of 1:50 by mass was carried out at a non-optimal temperature of 25°C for a short period of 1 hour. Under these conditions, fragments from exposed regions of the protein should be more accessible for digestion and hence detected at higher level, whereas fragments from shielded regions of the protein should be less accessible for digestion and hence detected at lower level. The samples were prepared in similar manner and the same amount of protein from each sample is used for relative comparison using MaxLFQ algorithm, integrated in the MaxQuant software.41

The relative intensity is reported for each fragment detected in each sample as a LFQ intensity value. Only fragments that were detected (reported with an LFQ intensity value) in at least 2 out of 3 replicates for each sample condition is considered valid. If a fragment is not detected at least 2 out of the 3 replicates, that fragment is considered not detected or has an LFQ intensity of 0. The average of log2-transformed LFQ intensity of all the fragments detected in free oPDI, 15 µg/mL oPDI: 0.005 nM AuNP, and 300 μg/mL oPDI: 0.005 nM AuNPs is shown in **Figure S3**. The average of log2-transformed LFQ intensity of all fragments detected in free rPDI, 15 µg/mL rPDI: 0.005 nM AuNP, and 300 μg/mL rPDI: 0.005 nM AuNPs are shown in Figure S4. The fragments are colored according to their relative quantification, where yellow illustrates high level and purple illustrates low level. The missing/not detected fragments are illustrated with white bars. As seen in Figure S3 and Figure S4, all fragment patterns for free and bound samples either for oPDI and rPDI are missing fragments from N-terminal regions up to position 88. This is plausibly because the digestion sites in this region are very close together, leaving digested fragments very short (1 to 6 amino acids (AA) in length), hence not detected by MaxQuant.42 However, majority of the missing region (AA residue 1-55) is only part of a N-terminal extension that is irrelevant to the main domain organization of bovine PDI, which includes the *a* (AA 79-191), *b* (AA 192-294), *b'* (AA 295-406), x-linker (AA 406-421), a' (AA 421-532), and Cterminal extension followed by the ER-retention sequence, KDEL.47

The same data is plotted as a heatmap shown in **Figure S5** to better highlight the missing fragments in some sample conditions. For example, the fragment containing residues 126-138 is not detected in all oPDI samples, while being detected in all rPDI samples. On the contrary, fragment containing residues 518-525 is detected in all oPDI samples, while not being detected in all rPDI samples. There are also fragments that is found in the free protein control while not being found after incubation with AuNPs, such as fragment containing residues 409-423 in oPDI samples and fragment containing residues 287-311 in rPDI samples. For both oPDI and rPDI, fragments containing residues 265-279 are detected in free samples and the 300 μg/mL PDI: 0.005 nM AuNPs samples while missing in the 15 μ g/mL PDI: 0.005 nM AuNPs samples. These results highlight the differences in oPDI and rPDI samples, free and bound protein samples as well as the role of incubation ratio play on the protein adsorption.

We then calculated the sum of all the averaged LFQ intensities across replicates of all detected fragments occurring at each digestion position. The ratio between those sums of the two sample types of interest for comparison is then computed and log₂-transformed to determine the fold change difference. We first compared free rPDI to oPDI, as shown in **Figure 5**. The points above zero represent digestion sites that are more accessible for digestion in free rPDI samples compared to free oPDI samples, the points below zero represent digestion sites that are less

accessible in free rPDI samples compared to free oPDI samples, and the points at zero represent digestion sites that are equally accessible in the free protein at both oxidation states. Most cut sites are less accessible in free rPDI samples in comparison to free oPDI samples. Table S1 highlights the digestion positions that are more accessible for digestion in free rPDI compared to free oPDI in green and those that are more shielded for digestion in orange. The digestion positions that are more exposed in free rPDI with respect to (wrt) free oPDI are concentrated on the a and a' region, suggesting the protein adopted a conformation where the b and b'regions are shielded from digestion enzyme. This is consistent with the closed conformation for rPDI reported in the literature, 2,5,6 which can limit the accessibility of the digestive enzyme. This result shows that oxidation state of the protein can dictate its accessibility to digestion, which in turns can have an effect upon adsorption onto NP surface.

We then compared the digestive patterns between the AuNP-exposed oPDI at 15 μ g/mL: 0.005 nM AuNP to the free oPDI and between the AuNP-exposed rPDI at 15 μ g/mL: 0.005 nM PDI: AuNP to the free rPDI resulting in the curves represented by the light blue squares and pink upside-down triangle, respectively, in **Figure 6A**.

Similarly, we also compared the digestive patterns between the AuNP-exposed oPDI at 300 µg/mL: 0.005 nM AuNP to the free oPDI and between the AuNP-exposed rPDI at 300 μg/mL: 0.005 nM AuNP to the free rPDI resulting in the curves represented by the blue circles and red triangle, respectively, in **Figure 6B**. The points above zero represents digestion positions that are more accessible on AuNP surface, the points below zero represent digestion positions that are less accessible on AuNP surface, and the points at zero represent digestion sites that are equally accessible in the free and on NP states. The digestion positions that are more exposed to digestion on NP surface are highlighted in green and the digestion positions that are more shielded from digestion on NP surface are highlighted in orange in Table S1. As seen in Figure 6 and Table S1, most digestion positions are more exposed to digestion position when adsorbed onto the NP surface, for both oPDI and rPDI. This shows that adsorption to the NP surface causes the protein to display differently to the digestive enzyme compared to the free protein. If a digestion position is not available in both free and bound states, that digestion is not valid for comparison, and they are highlighted by vertical black lines in Figure S3 and S4.

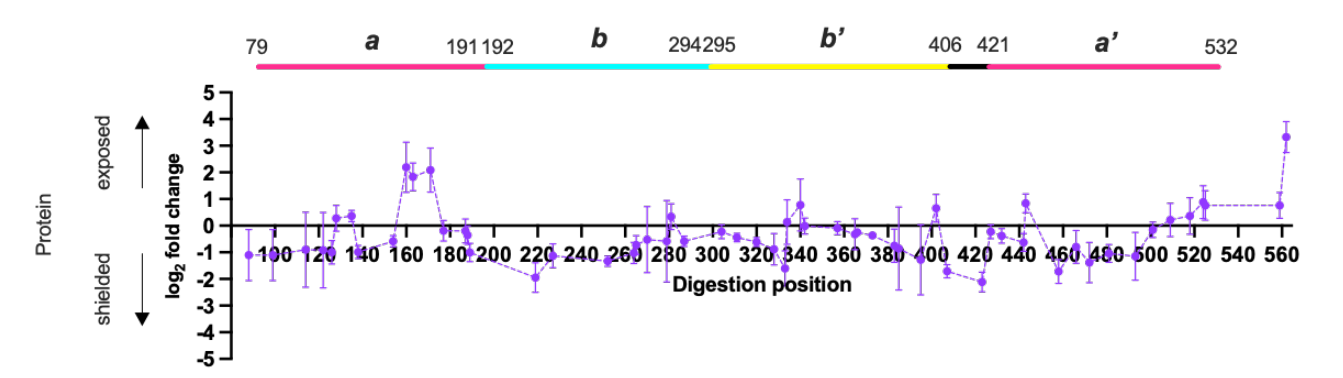


Figure 5. Exposure patterns showing digestion positions in free rPDI samples in comparison to free oPDI samples in log2-fold change. Points below zero show digestion positions that are more shieled in the free rPDI samples compared to the free oPDI samples. Points above zero show digestion positions that are more exposed in free rPDI samples compared to free oPDI samples. Points at zero represent digestion sites that are equally accessible in the free protein at both oxidation states Each data point represent average of 2-3 replicates and the error bars are standard deviation.

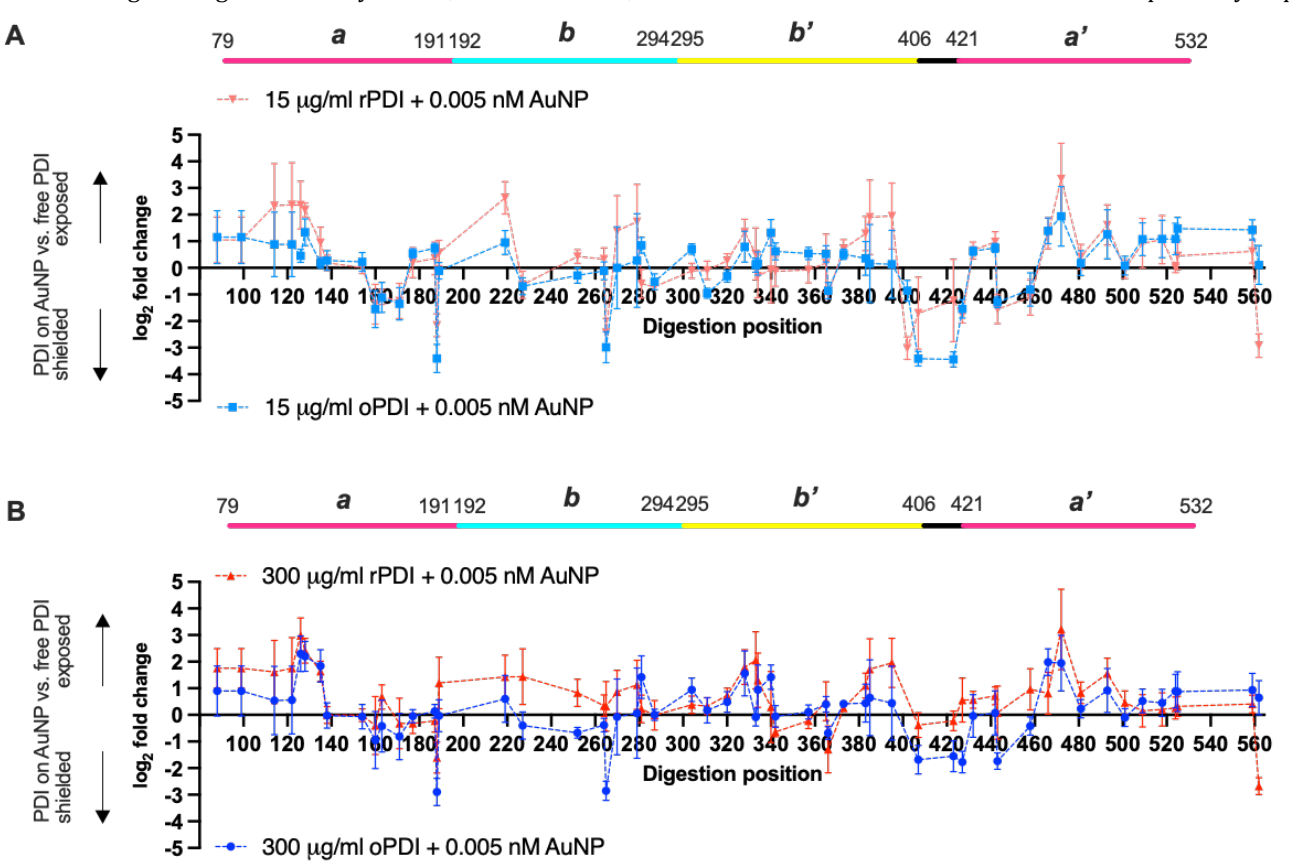
We utilized the PyMOL, an interactive protein structure visualization tool, to visualize the exposed (green) or shielded (orange) digestion position when oPDI or rPDI is on NP surface compared to the free counterparts using the bovine PDI structure predicted with AlphaFold (AF-F6Q9Q9-F1).48 We hypothesized that PDI is binding to AuNPs at the active sites -CGHC- at residues 110-113 (a domain) and residues 454-457 (a' domain) due to strong gold-thiol interactions.49,50 Although we cannot directly conclude that the fragments containing the active sites are more exposed or shielded from the digestive enzyme on NP surface because these specific fragments were not detected in any of the sample conditions, including the free PDI samples (Figure S3, S4, red vertical lines). We can, however, infer protein orientation on NP based on the level of exposure to digestion of other digestion positions.

As seen in **Figure 7** and **Figure S6**, most of the digestion positions that are more exposed to digestion on NP surface are located on α -helices that are outward facing, whereas most of the digestion positions that are more shielded from digestion on NP surface are located on β -sheets that are more buried. This result suggests that PDI adsorbs to the NP surface via the cysteines in the active sites so that all its regions (a, b, b', and a') are on the same plane. This orientation is plausible considering that the secondary structures of the protein did not alter significantly upon adsorption to NP surface (**Figure 4**). Moreover, this orientation can also explain the similar increase in AuNP hydrodynamic diameters upon oPDI and rPDI incubation (**Figure 1**).

We observed that several digestion positions in the b' region (K373, K383, K385, and K395) are more exposed to

digestion on NP in rPDI but not oPDI. This is interesting since this region neighbors two cysteines, C369 and C400,

conformation of oPDI/rPDI is retained upon adsorption to NP since the closed conformation of rPDI probably require



which are potentially additional anchoring sites for PDI on AuNP surface. This suggests that the open/closed sending this region outward (more exposed to digestion) to allow room for the cysteines to bind to AuNP surface.

Figure 6. Digestion patterns for AuNP-bound-oPDI (blue) with respect to the free oPDI and AuNP-bound-rPDI (red) with respect to the free rPDI at (A) incubation ratio of 15 μ g/mL PDI: 0.005 nM AuNP and at (B) incubation ratio of 300 μ g/mL PDI: 0.005 nM AuNP. Points below zero show digestion positions that are more shieled in the bound samples compared to the free samples. Points above zero show digestion positions that are more exposed in the bound samples compared to the free samples. Points at zero represent digestion sites that are equally accessible in the bound and in the free sample. Each data point represents average of 2-3 replicates and the error bars are standard deviation.

To further examine the discrepancy in the apparent protein thickness when incubating at low and high protein:AuNP ratios for oPDI and rPDI as seen in Figure 1, we analyzed the digestion patterns for oPDI (Figure 8A) and rPDI (**Figure 8B**) at 15 μg/mL PDI: 0.005 nM AuNP and $300~\mu g/mL$ PDI: 0.005~nM AuNP wrt to their free counterparts. The digestion patterns for low vs. high PDI: AuNP is generally more similar in oPDI samples while there is more discrepancy between incubation ratios in rPDI samples. There are some digestion positions that are more exposed to digestion in the low incubation ratio condition while being more shielded (or equally accessible) in the high incubation ratio condition (Table S2). For example, K320 is more shielded on NP at 15 μg/mL PDI: 0.005 nM AuNP while more exposed on NP at 300 μg/mL PDI: 0.005 nM AuNP for oPDI. On the other hand, K163, K227, and K458 is more shielded on NP at 15 μg/mL PDI: 0.005 nM AuNP while more exposed on NP at 300 μg/mL PDI: 0.005 nM AuNP for rPDI. This result is complementary to the DLS data, where there is not a significant difference between

the washed 15 µg/mL PDI: 0.005 nM AuNP and the washed 300 µg/mL PDI: 0.005 nM AuNP for oPDI, though there is a significant difference between the washed 15 µg/mL PDI: 0.005 nM AuNP and the washed 300 µg/mL PDI: 0.005 nM AuNP for rPDI (Figure 1). This result reiterates the role of oxidation state on protein binding on NP and highlights the role of incubation ratio has on the adsorption of the protein on NP surface. It appears that oPDI hard corona display on AuNP is similar at 15 μg/mL PDI: 0.005 nM AuNP and 300 μg/mL PDI: 0.005 nM AuNP, whereas the rPDI hard corona display differently at 15 μg/mL PDI: 0.005 nM AuNP and 300 µg/mL PDI: 0.005 nM AuNP. We postulate that the oxidation state of PDI modulates its adsorption onto the AuNP surface, and the first adsorbed layer of protein would then dictate the next layer of protein adsorption as the protein incubation ratio increases. $^{35,51,52}\,\mbox{The complex protein-protein interactions}$ in the hard and soft corona protein in rPDI is a probable cause for the differential protein display on NP surface.

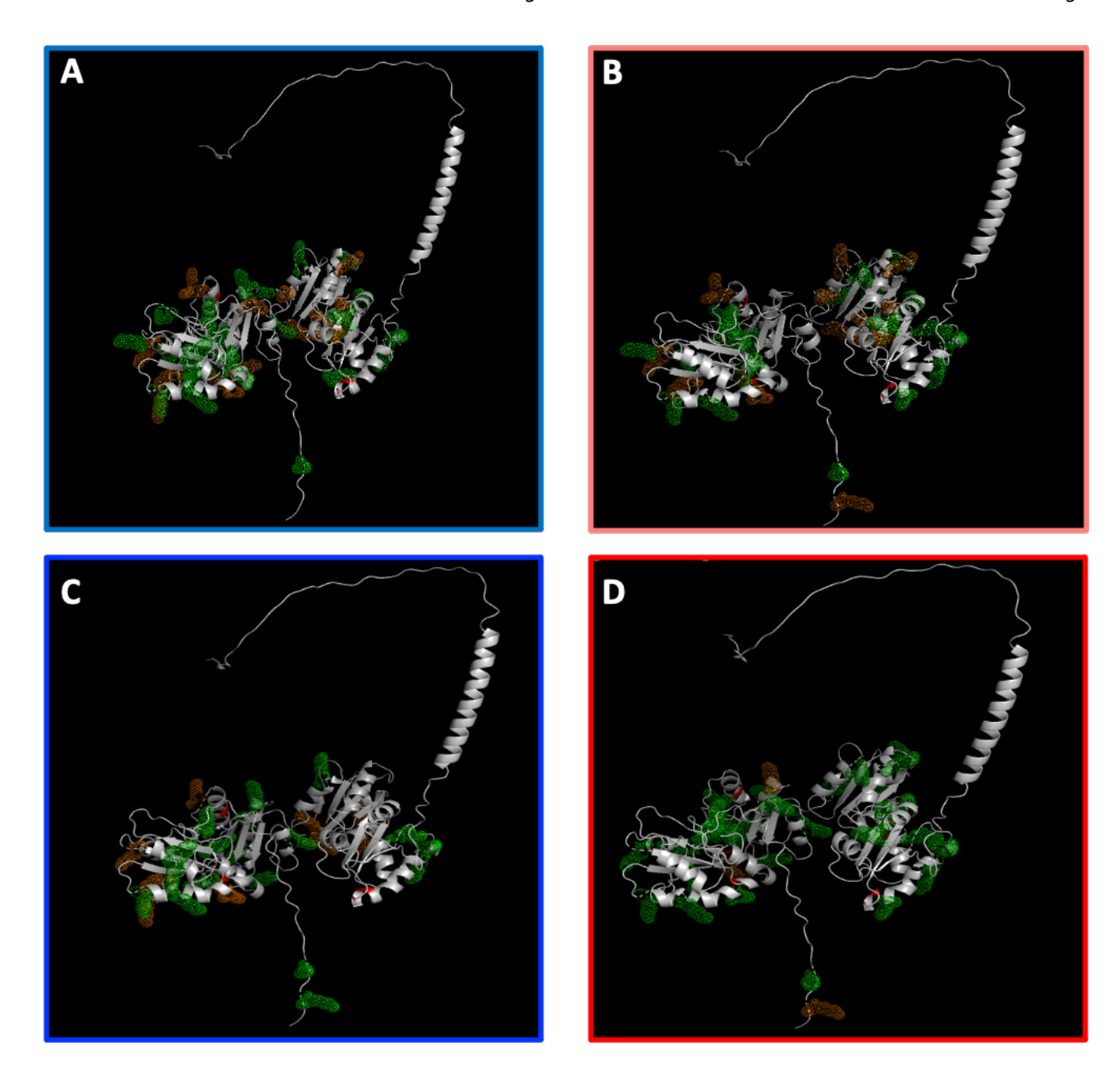


Figure 7. Protein structure visualization for (A, C) AuNP-bound-oPDI with respect to the free oPDI and (B,D) AuNP-bound-rPDI with respect to the free rPDI at incubation ratio of (A, B) 15 μ g/mL PDI: 0.005 nM AuNP and at incubation ratio of (C,D) 300 μ g/mL PDI: 0.005 nM AuNP, highlighting digestion positions that are more exposed (green) and shielded (orange) compared to free PDI when adsorbed to AuNP. Cysteines are highlighted in red. The PyMOL Molecular Graphics System, Version 2.0 Schrodinger, LLC.

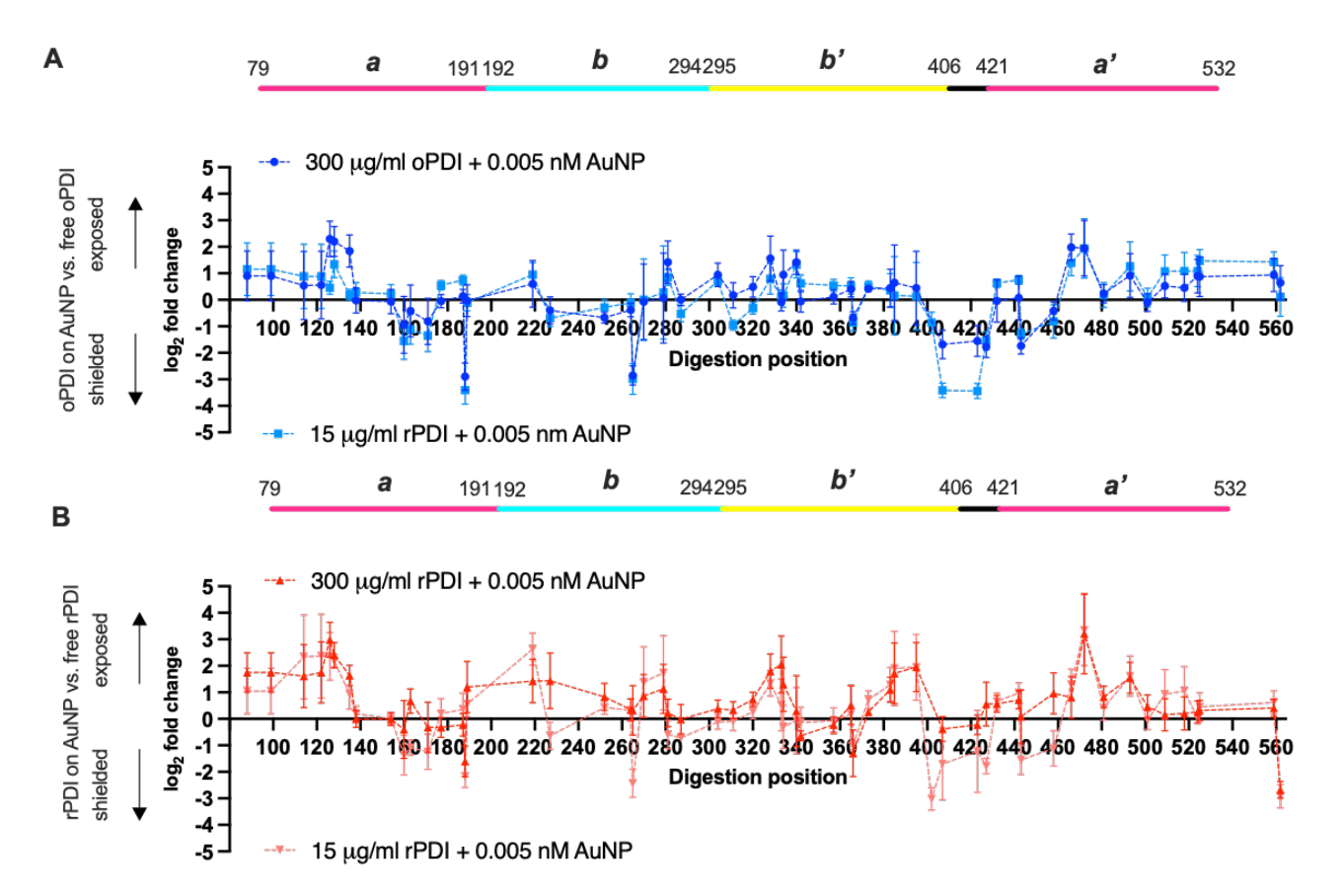


Figure 8. Digestion patterns for (A) AuNP-bound oPDI at $15 \mu g/mL$ oPDI: 0.005 nM AuNP (light blue squares) and $300 \mu g/mL$ oPDI: 0.005 nM AuNP (blue circle), and (B) AuNP-bound rPDI at $15 \mu g/mL$ rPDI: 0.005 nM AuNP (pink upside-down triangle) and $300 \mu g/mL$ rPDI: 0.005 nM AuNP (red triangles). Points below zero show digestion positions that are more shieled in the bound samples compared to the free samples. Points above zero show digestion positions that are more exposed in the bound samples compared to the free samples. Points at zero represent digestion sites that are equally accessible in the bound and in the free sample. Each data point represents average of 2-3 replicates and the error bars are standard deviation.

CONCLUSION

In this report, we have examined the interactions of PDI and AuNPs where the DLS titration, circular dichroism, and partial enzymatic digestion were used to probe the adsorption of the protein in either oxidized or reduced state to the AuNP surface. We found that oxidation state of the protein as well as incubation ratio of protein to NP modulate the final protein display on the surface. Adsorption to the NP surface did not seem to cause significant changes to the secondary structures distribution as observed by CD spectra. Partial enzymatic digestion experiments suggests that PDI can bound to AuNP at active sites cysteines in the a and a' region and the cysteines in the b'region, orienting all the protein regions on the same plane as NP surface, leading to increased accessibility to enzymatic digestion in various regions on the protein compared to the free counterpart. Binding to AuNP led to the reduction of bioavailability of PDI, as seen with the significant reduction in reductase and oxidoreductase/isomerase activity. Taken together, the data suggests NP can "knock out" PDI in vivo which can lead diminished maintenance of redox homostasis.53 This corroborates with other experiments where redox-nonactive AuNP induces oxidative stress. These experiments support the notion that NP

can interfere with cellular processes at the protein corona level. Additional experiments and modeling can aid the development for a clearer understanding of how this abundant protein and NPs interact and the potential downstream effects of these interactions to exploit its therapeutic potentials.

AUTHOR INFORMATION

Corresponding Author

Catherine J. Murphy* - Department of Chemistry, University of Illinois at Urbana- Champaign, 600 S Mathews Avenue, Urbana, IL 61801, United States; email: murphycj@illinois.edu; ORCID: 0000-0001-7066-5575

Authors

Khoi Nguyen L. Hoang - Department of Chemistry, University of Illinois at Urbana- Champaign, 600 S Mathews Avenue, Urbana, IL 61801, United States; email: klhoang2@illinois.edu; ORCID: 0000-0002-3822-4216

ASSOCIATED CONTENT

Supporting Information

Supplemental Information (PDF). Characterizations of AuNPs, raw DLS curves for PDI titration into AuNPs, fragmentation patterns and heatmaps for protein fragments detected in free protein and AuNP-exposed protein samples, additional protein structural

visualizations and summary of fold change level at each digestion position.

ACKNOWLEDGMENT

This material is based upon work supported by the National Science Foundation under Grant No. CHE-2001611, the NSF Center for Sustainable Nanotechnology. Electron microscopy was carried out at the Frederick Seitz Materials Research Laboratory Central Research Facilities, University of Illinois at Urbana-Champaign. We would like to thank Dr. Justine Arrington at the Proteomics Core Facility of the Roy J. Carver Biotechnology Center at the University of Illinois at Urbana-Champaign for the raw proteomic data.

REFERENCES

- (1) Wilkinson, B.; Gilbert, H. F. Protein Disulfide Isomerase. *Biochim. Biophys. Acta Proteins Proteomics* **2004**, *1699* (1–2), 35–44. https://doi.org/10.1016/j.bbapap.2004.02.017.
- (2) Ali Khan, H.; Mutus, B. Protein Disulfide Isomerase a Multifunctional Protein with Multiple Physiological Roles. *Front. Chem.* **2014**, *2*, 70. https://doi.org/10.3389/fchem.2014.00070.
- (3) Watanabe, M. M.; Laurindo, F. R. M.; Fernandes, D. C. Methods of Measuring Protein Disulfide Isomerase Activity: A Critical Overview. *Front. Chem.* **2014**, 2 (September), 73. https://doi.org/10.3389/fchem.2014.00073.
- (4) Wang, L.; Wang, X.; Wang, C. C. Protein Disulfide-Isomerase, a Folding Catalyst and a Redox-Regulated Chaperone. *Free Radic. Biol. Med.* **2015**, *83*, 305–313. https://doi.org/10.1016/j.freeradbiomed.2015.02.007.
- (5) Wang, C.; Li, W.; Ren, J.; Fang, J.; Ke, H.; Gong, W.; Feng, W.; Wang, C. Structural Insights into the Redox-Regulated Dynamic Conformations of Human Protein Disulfide Isomerase. *Antioxid. Redox Signal.* **2013**, *19* (1), 36–45. https://doi.org/10.1089/ars.2012.4630.
- (6) Yang, S.; Wang, X.; Cui, L.; Ding, X.; Niu, L.; Yang, F.; Wang, C.; Wang, C.; Lou, J. Compact Conformations of Human Protein Disulfide Isomerase. *PLoS One* **2014**, *9* (8), e103472. https://doi.org/10.1371/journal.pone.0103472.
- (7) Parakh, S.; Atkin, J. D. Novel Roles for Protein Disulphide Isomerase in Disease States: A Double Edged Sword? *Front. Cell Dev. Biol.* **2015**, *3*, 30. https://doi.org/10.3389/fcell.2015.00030.
- (8) Luo, B.; Lee, A. S. The Critical Roles of Endoplasmic Reticulum Chaperones and Unfolded Protein Response in Tumorigenesis and Anticancer Therapies. *Oncogene* **2013**, *32* (7), 805–818. https://doi.org/10.1038/onc.2012.130.
- (9) Hashida, T.; Kotake, Y.; Ohta, S. Protein Disulfide Isomerase Knockdown-Induced Cell Death Is Cell-Line-Dependent and Involves Apoptosis in MCF-7 Cells. *J. Toxicol. Sci.* **2011**, *36* (1), 1–7. https://doi.org/10.2131/jts.36.1.
- (10) Lovat, P. E.; Corazzari, M.; Armstrong, J. L.; Martin, S.; Pagliarini, V.; Hill, D.; Brown, A. M.; Piacentini, M.; Birch-Machin, M. A.; Redfern, C. P. F. Increasing Melanoma Cell Death Using Inhibitors of Protein Disulfide Isomerases to Abrogate Survival Responses to Endoplasmic Reticulum Stress. *Cancer Res.* **2008**, *68* (13), 5363–5369. https://doi.org/10.1158/0008-5472.CAN-08-0035.
- (11) Powell, L. E.; Foster, P. A. Protein Disulphide Isomerase Inhibition as a Potential Cancer Therapeutic Strategy. *Cancer Med.* **2021**, *10* (8), 2812–2825. https://doi.org/10.1002/cam4.3836.
- (12) Cheng, H.; Wang, L.; Wang, C. Domain a' of Protein Disulfide Isomerase Plays Key Role in Inhibiting α -Synuclein Fibril Formation. *Cell Stress Chaperones* **2010**, *15* (4), 415–421. https://doi.org/10.1007/s12192-009-0157-2.
- (13) Hoffstrom, B. G.; Kaplan, A.; Letso, R.; Schmid, R. S.; Turmel, G. J.; Lo, D. C.; Stockwell, B. R. Inhibitors of Protein Disulfide Isomerase Suppress Apoptosis Induced by Misfolded Proteins. *Nat. Chem. Biol.* **2010**, *6* (12), 900–906. https://doi.org/10.1038/nchembio.467.
- (14) Kaplan, A.; Gaschler, M. M.; Dunn, D. E.; Colligan, R.; Brown, L. M.; Palmer, A. G.; Lo, D. C.; Stockwell, B. R. Small Molecule-Induced Oxidation of Protein Disulfide Isomerase Is

Neuroprotective. *Proc. Natl. Acad. Sci.* **2015**, *112* (17), E2245–E2252. https://doi.org/10.1073/pnas.1500439112.

- (15) Zwicker, J. I.; Schlechter, B. L.; Stopa, J. D.; Liebman, H. A.; Aggarwal, A.; Puligandla, M.; Caughey, T.; Bauer, K. A.; Kuemmerle, N.; Wong, E.; Wun, T.; McLaughlin, M.; Hidalgo, M.; Neuberg, D.; Furie, B.; Flaumenhaft, R. Targeting Protein Disulfide Isomerase with the Flavonoid Isoquercetin to Improve Hypercoagulability in Advanced Cancer. *JCI Insight* **2019**, *4* (4), E125851. https://doi.org/10.1172/jci.insight.125851.
- (16) Murphy, C. J.; Vartanian, A. M.; Geiger, F. M.; Hamers, R. J.; Pedersen, J.; Cui, Q.; Haynes, C. L.; Carlson, E. E.; Hernandez, R.; Klaper, R. D.; Orr, G.; Rosenzweig, Z. Biological Responses to Engineered Nanomaterials: Needs for the Next Decade. *ACS Cent. Sci.* **2015**, *1* (3), 117–123. https://doi.org/10.1021/acscentsci.5b00182.
- (17) Maurer-Jones, M. A.; Gunsolus, I. L.; Murphy, C. J.; Haynes, C. L. Toxicity of Engineered Nanoparticles in the Environment. *Anal. Chem.* **2013**, *85* (6), 3036–3049. https://doi.org/10.1021/ac303636s.
- (18) Hochella, M. F.; Mogk, D. W.; Ranville, J.; Allen, I. C.; Luther, G. W.; Marr, L. C.; McGrail, B. P.; Murayama, M.; Qafoku, N. P.; Rosso, K. M.; Sahai, N.; Schroeder, P. A.; Vikesland, P.; Westerhoff, P.; Yang, Y. Natural, Incidental, and Engineered Nanomaterials and Their Impacts on the Earth System. *Science* (80-.). **2019**, 363 (6434), eaau8299. https://doi.org/10.1126/science.aau8299.
- (19) Vance, M. E.; Kuiken, T.; Vejerano, E. P.; McGinnis, S. P.; Hochella, M. F.; Hull, D. R. Nanotechnology in the Real World: Redeveloping the Nanomaterial Consumer Products Inventory. *Beilstein J. Nanotechnol.* **2015**, *6* (1), 1769–1780. https://doi.org/10.3762/bjnano.6.181.
- (20) Murphy, C. J.; Chang, H.-H.; Falagan-Lotsch, P.; Gole, M. T.; Hofmann, D. M.; Hoang, K. N. L.; McClain, S. M.; Meyer, S. M.; Turner, J. G.; Unnikrishnan, M.; Wu, M.; Zhang, X.; Zhang, Y. Virus-Sized Gold Nanorods: Plasmonic Particles for Biology. *Acc. Chem. Res.* **2019**, *52* (8), 2124–2135. https://doi.org/10.1021/acs.accounts.9b00288.
- (21) Rastinehad, A. R.; Anastos, H.; Wajswol, E.; Winoker, J. S.; Sfakianos, J. P.; Doppalapudi, S. K.; Carrick, M. R.; Knauer, C. J.; Taouli, B.; Lewis, S. C.; Tewari, A. K.; Schwartz, J. A.; Canfield, S. E.; George, A. K.; West, J. L.; Halas, N. J. Gold Nanoshell-Localized Photothermal Ablation of Prostate Tumors in a Clinical Pilot Device Study. *Proc. Natl. Acad. Sci. U. S. A.* **2019**, *116* (37), 18590–18596. https://doi.org/10.1073/pnas.1906929116.
- (22) Vines, J. B.; Yoon, J. H.; Ryu, N. E.; Lim, D. J.; Park, H. Gold Nanoparticles for Photothermal Cancer Therapy. *Front. Chem.* **2019**, *7*, 167. https://doi.org/10.3389/fchem.2019.00167.
- (23) Wu, Y.; Ali, M. R. K.; Chen, K.; Fang, N.; El-Sayed, M. A. Gold Nanoparticles in Biological Optical Imaging. *Nano Today* **2019**, *24*, 120–140. https://doi.org/10.1016/j.nantod.2018.12.006.
- (24) Hu, X.; Zhang, Y.; Ding, T.; Liu, J.; Zhao, H. Multifunctional Gold Nanoparticles: A Novel Nanomaterial for Various Medical Applications and Biological Activities. *Front. Bioeng. Biotechnol.* **2020**, 8, 990. https://doi.org/10.3389/fbioe.2020.00990.
- (25) Kus-Liśkiewicz, M.; Fickers, P.; Ben Tahar, I. Biocompatibility and Cytotoxicity of Gold Nanoparticles: Recent Advances in Methodologies and Regulations. *Int. J. Mol. Sci.* **2021**, *22* (20), 10952. https://doi.org/10.3390/ijms222010952.
- (26) Enea, M.; Pereira, E.; Peixoto de Almeida, M.; Araújo, A. M.; Bastos, M. de L.; Carmo, H. Gold Nanoparticles Induce Oxidative Stress and Apoptosis in Human Kidney Cells. *Nanomaterials* **2020**, *10*, 995. https://doi.org/10.3390/nano10050995.
- (27) Jawaid, P.; Rehman, M. U.; Zhao, Q.; Misawa, M.; Ishikawa, K.; Hori, M.; Shimizu, T.; Saitoh, J.; Noguchi, K.; Kondo, T. Small Size Gold Nanoparticles Enhance Apoptosis-Induced by Cold Atmospheric Plasma via Depletion of Intracellular GSH and Modification of Oxidative Stress. *Cell Death Discov.* **2020**, *6*, 83. https://doi.org/10.1038/s41420-020-00314-x.
- (28) Li, J. J.; Lo, S.; Ng, C.; Gurung, R. L.; Hartono, D.; Hande, M. P.; Ong, C.; Bay, B.; Yung, L. L. Genomic Instability of Gold Nanoparticle Treated Human Lung Fibroblast Cells. *Biomaterials*

- , 32 (23), 5515–5523. https://doi.org/10.1016/j.biomaterials.2011.04.023.
- (29) Falagan-Lotsch, P.; Grzincic, E. M.; Murphy, C. J. One Low-Dose Exposure of Gold Nanoparticles Induces Long-Term Changes in Human Cells. *Proc. Natl. Acad. Sci. U. S. A.* **2016**, *113* (47), 13318–13323. https://doi.org/10.1073/pnas.1616400113.
- (30) Wheeler, K. E.; Chetwynd, A. J.; Fahy, K. M.; Hong, B. S.; Tochihuitl, J. A.; Foster, L. A.; Lynch, I. Environmental Dimensions of the Protein Corona. *Nat. Nanotechnol.* **2021**, *16* (6), 617–629. https://doi.org/10.1038/s41565-021-00924-1.
- (31) Fleischer, C. C.; Payne, C. K. Nanoparticle Surface Charge Mediates the Cellular Receptors Used by Protein-Nanoparticle Complexes. *J. Phys. Chem. B* **2012**, *116* (30), 8901–8907. https://doi.org/10.1021/jp304630q.
- (32) Walczyk, D.; Bombelli, F. B.; Monopoli, M. P.; Lynch, I.; Dawson, K. A. What the Cell "Sees" in Bionanoscience. *J. Am. Chem. Soc.* **2010**, *132* (16), 5761–5768. https://doi.org/10.1021/ja910675v.
- (33) Salvati, A.; Pitek, A. S.; Monopoli, M. P.; Prapainop, K.; Bombelli, F. B.; Hristov, D. R.; Kelly, P. M.; Åberg, C.; Mahon, E.; Dawson, K. A. Transferrin-Functionalized Nanoparticles Lose Their Targeting Capabilities When a Biomolecule Corona Adsorbs on the Surface. *Nat. Nanotechnol.* **2013**, 8 (2), 137–143. https://doi.org/10.1038/nnano.2012.237.
- (34) Yue, Y.; Behra, R.; Sigg, L.; Suter, M. J. F.; Pillai, S.; Schirmer, K. Silver Nanoparticle-Protein Interactions in Intact Rainbow Trout Gill Cells. *Environ. Sci. Nano* **2016**, *3* (5), 1174–1185. https://doi.org/10.1039/c6en00119j.
- (35) Hoang, K. N. L.; Wheeler, K. E.; Murphy, C. J. Isolation Methods Influence the Protein Corona Composition on Gold-Coated Iron Oxide Nanoparticles. *Anal. Chem.* **2022**, *94* (11), 4737–4746. https://doi.org/10.1021/acs.analchem.1c05243.
- (36) Perrault, S. D.; Chan, W. C. W. Synthesis and Surface Modification of Highly Monodispersed, Spherical Gold Nanoparticles of 50–200 Nm. *J. Am. Chem. Soc.* **2009**, *131* (47), 17042–17043. https://doi.org/10.1021/ja907069u.
- (37) Compton, L. A.; Johnson Jr., W. C. Analysis of Protein Circular Dichroism Spectra for Secondary Structure Using a Simple Matrix Multiplication. *Anal. Biochem.* **1986**, *155*, 155–167.
- (38) Whitmore, L.; Wallace, B. A. Protein Secondary Structure Analyses from Circular Dichroism Spectroscopy: Methods and Reference Databases. *Biopolymers* **2008**, *89* (5), 392–400. https://doi.org/10.1002/bip.20853.
- (39) Smith, A. M.; Chan, J.; Oksenberg, D.; Urfer, R.; Wexler, D. S.; Ow, A.; Gao, L.; McAlorum, A.; Huang, S. A High-Throughput Turbidometric Assay for Screening Inhibitors of Protein Disulfide Isomerase Activity. *SLAS Discov.* **2004**, *9* (7), 614–620. https://doi.org/10.1177/1087057104265292.
- (40) Lyles, M. M.; Gilbert, H. F. Catalysis of the Oxidative Folding of Ribonuclease a by Protein Disulfide Isomerase: Dependence of the Rate on the Composition of the Redox Buffer. *Biochemistry* **1991**, *30* (3), 619–625.
- (41) Cox, J.; Hein, M. Y.; Luber, C. A.; Paron, I.; Nagaraj, N.; Mann, M. Accurate Proteome-Wide Label-Free Quantification by Delayed Normalization and Maximal Peptide Ratio Extraction, Termed MaxLFQ. *Mol. Cell. Proteomics* **2014**, *13* (9), 2513–2526. https://doi.org/10.1074/mcp.M113.031591.
- (42) Tyanova, S.; Temu, T.; Cox, J. The MaxQuant Computational Platform for Mass Spectrometry-Based Shotgun

- Proteomics. *Nat. Protoc.* **2016**, *11* (12), 2301–2319. https://doi.org/10.1038/nprot.2016.136.
- (43) Yang, J. A.; Johnson, B. J.; Wu, S.; Woods, W. S.; George, J. M.; Murphy, C. J. Study of Wild-Type α-Synuclein Binding and Orientation on Gold Nanoparticles. *Langmuir* **2013**, *29* (14), 4603–4615. https://doi.org/10.1021/la400266u.
- (44) McClain, S. M.; Ojoawo, A. M.; Lin, W.; Rienstra, C. M.; Murphy, C. J. Interaction of Alpha-Synuclein and Its Mutants with Rigid Lipid Vesicle Mimics of Varying Surface Curvature. *ACS Nano* **2020**, *14* (8), 10153–10167. https://doi.org/10.1021/acsnano.0c03420.
- (45) Zheng, T.; Cherubin, P.; Cilenti, L.; Teter, K.; Huo, Q. A Simple and Fast Method to Study the Hydrodynamic Size Difference of Protein Disulfide Isomerase in Oxidized and Reduced Form Using Gold Nanoparticles and Dynamic Light Scattering. *Analyst* **2016**, *141* (3), 934–938. https://doi.org/10.1039/c5an02248g.
- (46) Guyette, J.; Evangelista, B.; Tatulian, S. A.; Teter, K. Stability and Conformational Resilience of Protein Disulfide Isomerase. *Biochemistry* **2019**, *58* (34), 3572–3584. https://doi.org/10.1021/acs.biochem.9b00405.
- (47) Tian, G.; Xiang, S.; Noiva, R.; Lennarz, W. J.; Schindelin, H. The Crystal Structure of Yeast Protein Disulfide Isomerase Suggests Cooperativity between Its Active Sites. *Cell* **2006**, *124* (1), 61–73. https://doi.org/10.1016/j.cell.2005.10.044.
- (48) Jumper, J.; Evans, R.; Pritzel, A.; Green, T.; Figurnov, M.; Ronneberger, O.; Tunyasuvunakool, K.; Bates, R.; Žídek, A.; Potapenko, A.; Bridgland, A.; Meyer, C.; Kohl, S. A. A.; Ballard, A. J.; Cowie, A.; Romera-Paredes, B.; Nikolov, S.; Jain, R.; Adler, J.; Back, T.; Petersen, S.; Reiman, D.; Clancy, E.; Zielinski, M.; Steinegger, M.; Pacholska, M.; Berghammer, T.; Bodenstein, S.; Silver, D.; Vinyals, O.; Senior, A. W.; Kavukcuoglu, K.; Kohli, P.; Hassabis, D. Highly Accurate Protein Structure Prediction with AlphaFold. *Nature* **2021**, *596* (7873), 583–589. https://doi.org/10.1038/s41586-021-03819-2.
- (49) Taggart, L. E.; McMahon, S. J.; Butterworth, K. T.; Currell, F. J.; Schettino, G.; Prise, K. M. Protein Disulphide Isomerase as a Target for Nanoparticle-Mediated Sensitisation of Cancer Cells to Radiation. *Nanotechnology* **2016**, *27* (21), 215101. https://doi.org/10.1088/0957-4484/27/21/215101.
- (50) Hinman, J. G.; Eller, J. R.; Lin, W.; Li, J.; Li, J.; Murphy, C. J. Oxidation State of Capping Agent Affects Spatial Reactivity on Gold Nanorods. *J. Am. Chem. Soc.* **2017**, *139* (29), 9851–9854. https://doi.org/10.1021/jacs.7b06391.
- (51) Zhang, Y.; Wu, J. L. Y.; Lazarovits, J.; Chan, W. C. W. An Analysis of the Binding Function and Structural Organization of the Protein Corona. *J. Am. Chem. Soc.* **2020**, *142* (19), 8827–8836. https://doi.org/10.1021/jacs.0c01853.
- (52) Wang, C.; Chen, B.; He, M.; Hu, B. Composition of Intracellular Protein Corona around Nanoparticles during Internalization. *ACS Nano* **2021**, *15* (2), 3108–3122. https://doi.org/10.1021/acsnano.0c09649.
- (53) Zhang, X.; Falagan-Lotsch, P.; Murphy, C. J. Nanoparticles Interfere with Chemotaxis: An Example of Nanoparticles as Molecular "Knockouts" at the Cellular Level. *ACS Nano* **2021**, *15* (5), 8813–8825. https://doi.org/10.1021/acsnano.1c01262.

TOC GRAPHIC

